Recent Advances in Observation and Research of the Chinese Meridian Project

WANG Chi

(State Key Laboratory of Space Weather, National Space Science Center, Chinese Academy of Sciences, Beijing 100190)

Abstract

The Chinese Meridian Space Weather Monitoring Project (Meridian Project) is a ground-based geospace monitoring chain in China. It consists of 15 ground-based observation stations located roughly along 120°E longitude and 30°N latitude. In recent two years, using data from the Meridian Project, significant progresses have been made in space weather and space physics research. These advances are mainly in four aspects: regional characteristics of space environment above China or along 120°E meridian line, coupling between space spheres at different heights and different physical processes, space weather disturbance and its propagation along the meridian chain, and space weather effects on ground technical facilities.

Key words

Meridian Project, Ground-based observation, Space Weather, Solar-terrestrial physics

E-mail: cw@spaceweather.ac.cn

1. Overview of the Chinese Meridian Project

Since magnetic field lines in the near earth environment roughly align with meridian lines, and radiation from the sun presents a zenith angle effect along latitude direction, many physical processes occur along meridian lines and space environment characteristic has strong dependence on latitude. It has very important scientific significance to measure space environment parameters along meridian lines. The Chinese Meridian Project was proposed based on this idea, taking advantage of large latitude span of China's territory, which covers low to middle magnetic latitude (Chi Wang. [2010]).

With the full name of East-hemisphere Space Environment Ground-based Comprehensive Monitoring Chain, the project consists of chains of 15 ground-based observatories located roughly along 120°E longitude and 30°N latitude. One chain of observatories starts from Mohe, the northernmost city of China, and runs south roughly through Beijing, Wuhan, Guangzhou, and the island of Hainan (with instruments at Hikou, Fuke, and Sanya) and extends to China's Zhongshan station in Antarctica (see Figure 1). Distances between neighbouring stations are roughly 4°–5° of latitude, or about 500 kilometers near 120°E longitude, except the Zhongshan station in Antarctica. A chain of stations was also constructed roughly following 30°N, spanning from Lhasa to Shanghai. Each observatory is equipped with multiple instruments to comprehensively measure key parameters such as the baseline and time-varying geomagnetic field, as well as the middle and upper atmosphere and ionosphere from about 20 to 1000 kilometers. Parameters of solar wind are also tentatively measured.

Besides the space environment monitoring system that comprises instruments, a Data & Communication System and a Research & Forecasting System were also built, which located in Beijing. The Data & Communications System is in charge of collecting, transferring, processing, storing, and distributing data in quasi real time. All data is made public via the website data. meridianproject.ac.cn. The Research & Forecasting System coordinates observations, develops relevant data analysis and space weather forecasting tools, and promotes international collaborations.

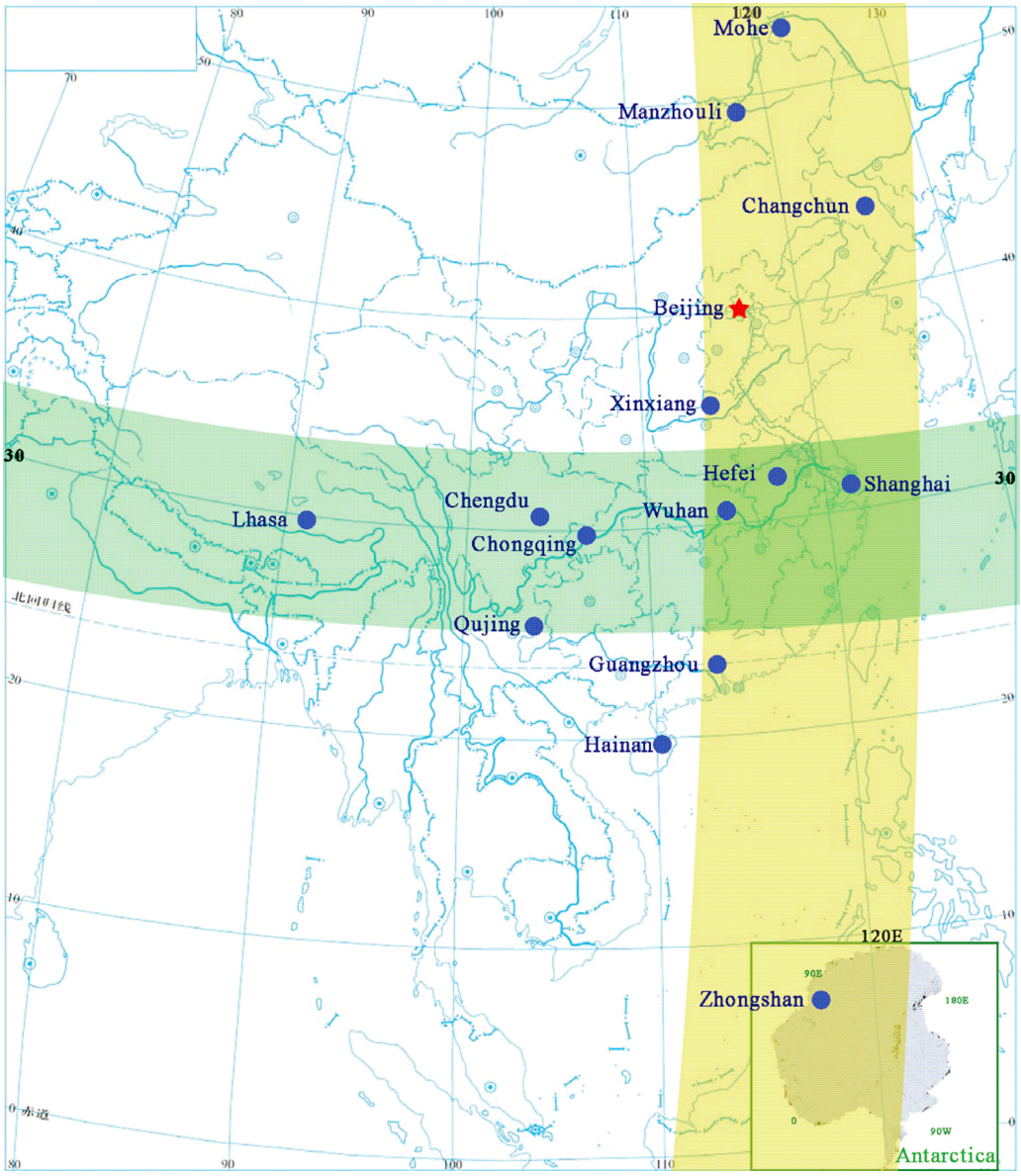

Fig. 1 Distribution of observatories that form the Meridian Project (yellow band traces stations along 120°E; green band shows stations close to 30°N) (from Chi Wang [2010])

Funded by China's National Development and Reform Commission as a part of a series of major scientific infrastructures, the budget of the Chinese Meridian Project is about 167 million yuan, or 24 million US dollars according to exchange rate of the day. Construction of the project started in January 2008 and completed in December 2012. It is a joint effort of 12 institutions or universities in China, led by National Space Science Center (NSSC), Chinese Academy of Sciences.

2. Instruments

Instruments of the Meridian Project mainly include magnetometers, traditional and digital ionosondes, digisondes, incoherent scatter radars, high-frequency backscatter radars, mesosphere-stratosphere-troposphere radars, meteor radars, lidar (light detection and ranging), Fabry- Perot Interferometers (FPI), and aurora spectrographs. Overall, the instruments can be grouped into four categories, named geomagnetic (geoelectric) field, radio wave, optical, and sounding rocket. Altogether, 87 instruments were built and installed at 15 stations. The precise locations of stations along with the types of instruments that installed at each are listed in Table 1.

Table 1 Station locations, along with instruments deployed at each

Station	Latitude	Longitude	Instruments
Mohe	53.5°N	122.4°E	digisonde, GPS-TEC[a] monitor, meteor radar, fluxgate magnetometer, fluxgate theodolite, overhauser magnetometer, coil magnetometer, atmosphere electric instrument
Manzhouli	49.6°N	117.4°E	fluxgate magnetometer, coil magnetometer, geoelectric instrument, ionosonde
Changchun	44.0°N	125.2°E	fluxgate magnetometer, coil magnetometer, geoelectric instrument, atmosphere electric instrument, ionosonde
Beijing[c]	40.3°N	116.2°E	fluxgate magnetometer, coil magnetometer, fluxgate theodolite, overhauser magnetometer, digisonde, lidar,[b] all- sky airglow imager, Fabry-Perot interferometer, mesosphere-stratosphere-thermosphere radar, interplanetary scintillation monitor, cosmic ray monitor, TEC and ionospheric scintillation monitor, high-frequency Doppler frequency shift monitor, GPS-TEC monitor
Xinxiang[c]	34.6°N	113.6°E	fluxgate magnetometer, coil magnetometer, GPS-TEC monitor
Hefei	33.4°N	116.5°E	lidar
Wuhan[c]	30.5°N	114.6°E	fluxgate magnetometer, coil magnetometer, geoelectric instrument , atmosphere electric instrument , digisonde, lidar, mesosphere-stratosphere-thermosphere radar, meteor radar, GPS-TEC monitor
Guangzhou[c]	23.1°N	113.3°E	fluxgate magnetometer, coil magnetometer, geoelectric instrument, atmosphere electric instrument, ionosonde, cosmic ray telescope, TEC and ionospheric scintillation monitor, high-frequency Doppler frequency shift monitor
Hainan[c]	19.0°N	109.8°E	fluxgate magnetometer, coil magnetometer, fluxgate theodolite, overhauser magnetometer, digisonde, GPS-TEC monitor, lidar, all-sky airglow imager, very high frequency radar, sounding rockets
Zhongshan	69.4°S	76.4°E	fluxgate magnetometer, fluxgate theodolite, overhauser magnetometer, digisonde, high-frequency coherent scatter radar, aurora spectrometer
Shanghai	31.1°N	121.2°E	fluxgate magnetometer, coil magnetometer
Chongqing	29.5°N	106.5°E	ionosonde
Chengdu	31.0°N	103.7°E	fluxgate magnetometer, coil magnetometer, atmosphere electric instrument, geoelectric instrument
Qujing	25.6°N	103.8°E	incoherent scatter radar
Lhasa	29.6°N	91.0°E	fluxgate magnetometer, coil magnetometer

[a] Total electron content.
[b] Light detection and ranging.
[c] Instruments were deployed at multiple sites. Precise location of each site not listed.

3. Recent Advances of Observation and Research

The Meridian Project was put into formal operation in December, 2012. To the end of 2017, 13880 thousand data files (5.05 TB) have been accumulated. Exploring these data, scientists published more than 200 papers making significant progresses in space physics and space weather research. More than 10 national or provincial level awards were obtained, of which 'the driving process of ionosphere variation' made by the in-house team won two Second Class Prizes of National Natural Science Award of China. In the following paragraphs, research progress in recent two years (2016 to 2017) will be summarized and briefly introduced.

3.1 Regional Characteristics of Space Environment

Detecting the changing of the upper atmosphere is an important and challenging task. Liu *et al*. [2017a] used the observations from the VHF all-sky meteor radars operated at Beijing and Mohe, China to explore the temporal patterns of the meteor peak heights. They found that there were considerable seasonal variations in the meteor peak heights, being dominated by an annual component at Beijing and a semiannual component at Mohe. Moreover, the Ensemble Empirical Mode Decomposition (EEMD) revealed an overall decrease in the meteor peak heights at both stations, indicating the descending trend in neutral density near 90 km altitude at middle latitudes. The meteor peak heights showed a rather weak solar activity dependence at Beijing, which was different from the positive dependence reported at some other sites.

Also by the VHF all-sky meteor radar operated at Mohe, Liu *et al*. [2017b] made an estimation of mesospheric temperature at 90 km height. The results showed that the temperature presented a considerable annual

variation, with maximum in winter and minimum in summer. Harmonic analysis showed that the temperature had an annual variation consistent with the SABER temperature (TSABER) on board the TIMED satellite. The Full Width at Half Maximum (FWHM) of the meteor height had a good performance in routine estimation of the mesospheric temperatures.

Using multiple detection methods of the Meridian Project, the wind climatology in mesosphere and lower thermosphere (80–110 km) over central China was studied by a comparison between measurements by a Fabry-Perot Interferometer (FPI) and a Meteor Radar (MR), that located at two stations about 400km apart [Yu *et al*., 2016]. The results showed the MR and FPI winds roughly rotate uniformly in a clockwise direction with a period of about 24 h and with velocities in range of 10-50 m/s. At 87 km, the FPI and MR winds agreed with each other very well in all months. At 97 km, the FPI and MR winds agreed with each other from May to October and were obviously different in the rest months.

In the mesosphere and lower thermosphere, there are different neutral metal atom layers with different elements, including sodium, potassium, and calcium. Sporadic sodium layer (SSL or NaS) is a mesospheric phenomenon in which the density of sodium layer could be more than double the background value within a very short time (*e.g*. within 5 min) in a narrow altitude range. Qiu *et al*. [2016] used the observations from the lidars operated at Hefei and Haikou to study the latitudinal characteristics of SSLs. The results highlighted both the single-mechanism and combined actions of the temperature mechanism and E_S theory on the formation of the SSLs in different latitudes and altitudes. The high latitude SSLs had a closer link with the E_S theory and the subtropical SSLs correlate more strongly to high temperature, while both the temperature mechanism and E_S theory probably contributed equally to the SSLs in the low-latitude Haikou station. The observations in Haikou also showed that two SSL events could be controlled by different mechanisms even though they occurred at the same location within the same night.

To date, extensive research has been carried out on sodium layers but studies on potassium (K) layers are rare. A main reason is that because the potassium column abundance is about 2 orders of magnitude smaller than that of sodium. However, observations of potassium layers are very important for the studies of upper atmosphere chemistry and cosmic dust. Jiao *et al*. [2017] reported highly concentrated layers of atomic K in the mesosphere above Yanqing near Beijing. In these narrow layers, the K density exceeded 1100 cm^{-3}. They used a model with detailed metal ion chemistry to show these sporadic K layers could be produced from a strong sporadic E layer that descended from above 100 km. Most of Na^+ ions were neutralized before the remaining ions were dumped around 90 km, where the higher pressures and colder temperatures facilitated the formation of $K^+.N_2$ and $K^+.CO_2$ cluster ions. These cluster ions then undergo dissociative recombination with electrons to form K.

Wang *et al*. [2017] studied seasonal variations of meteoric potassium layers over Beijing. The potassium layer showed considerable semiannual seasonal variations. Specifically, the column and peak densities varied semiannually, with maxima in winter and summer. The centroid height indicated semiannual variation reaching maxima in spring and autumn. The Root Mean Square (RMS) width had a slight semiannual seasonality with maxima in July and December. The seasonal behavior of the potassium layer in Beijing was similar to that in other potassium lidar sites. A significant difference is that the column and peak densities of the potassium layer in winter are extremely large, compared to the other maximum in summer.

Aside from upper atmosphere, progresses were also made for study of lower atmosphere using the observation of the Meridian Project. Huang *et al*. [2017] studied the Planetary Waves (PWs) characteristics in the lower atmosphere revealed by the Beijing MST radar and Modern Era Retrospective analysis for Research and Applications (MERRA) data. Their results showed that the dominant planetary waves (quasi-16-day and quasi-10-day oscillations) displayed similar seasonal and height variations. For both of them, significant zonal amplitudes were observed in winter and spring months near the tropospheric jet; quasi-constant phase or partial vertical wavelength larger than 100 km was present in the zonal wind in December, March, and April, indicating that they were quasi vertical standing waves near the tropospheric jet. Furthermore, they investigated the impact of PWs on the background wind by Eliassen-Palm fluxes and divergences. The quasi-16-day and the quasi-10-day PWs might contribute significantly to the construction and maintenance of the tropospheric jet,

especially the latter. They found that the quasi-16-day and quasi-10-day PWs could modulate tropospheric jet magnitude and height intensively.

Using observations by the lidars and radiosondes at Wuhan, China, Wu *et al.* [2017] studied the local ice formation via liquid water growth in slowly ascending humid aerosol/liquid water layers that occurred at altitudes of 2–4 km in winter. The study showed that, with a slow ascent, the layer developed into a nearly opaque liquid cloud layer and then ice crystals abruptly formed at the upper edge of the cloud layer with very high liquid water content. The ice crystals likely came from water drop freezing. The freezing temperatures estimated from radiosonde measurements were –3 to –8°C. For two available long-lived (>16 h) cases, the layer was observed to always lie just below an inversion layer. The ice development on the layer was followed by rainfall.

For ionosphere, an abundance of physical processes and phenomenon can be studied by using the instruments of the Meridian Project. Zhou *et al.* [2017] studied the characteristics of sporadic E layer using the data at four ionospheric sounding stations of Mohe, Beijing, Wuhan, and Hainan, China. Consistent with previous studies, the occurrence of the sporadic E layer in mid-latitude China region showed strong dependence on local time and season. At local daytime in summer season, the occurrence of the mid-latitude sporadic E layer was conspicuous. The results also showed that the post-sunset sporadic E layer was statistically pronounced in mid-latitude China region, possibly related to the nighttime E region irregularities.

Li *et al.* [2016] studied the characteristics of the DC electric field in the F1-region (between 130 and 190 km) by a sounding rocket launched at Hainan station. A set of electric field double probes measured the DC electric field during 05:45–05:52 LT on April 5, 2013. The data revealed a special profile in which the vectors of the DC electric field vary with altitude between 130 and 190 km. This is the first in situ measurement of the DC electric field conducted within the F1-region in the East Asian Sector.

Equatorial Plasma Bubbles (EPBs) are nighttime ionospheric structures in F region. They are usually associated with Equatorial Spread F (ESF) or plume structures. Sun *et al.* [2016] studied equatorial plasma bubble structures based on a network of four all-sky airglow imagers in the Chinese longitudinal sector (94.0° to 118.0°E in longitude). For the first time they used nearly 3 years of airglow data to study the statistical features of EPBs, including seasonal and daily occurrence rates and the influence of solar activity on the occurrence rate. EPBs mainly occurred during 21:00 LT–00:00 LT in equinoxes. There was an asymmetry in occurrence rates between March (June) and September equinoxes (December solstices).

By observations from two all-sky airglow imagers located in the magnetically equatorial region of Hainan and Guiping, China, Wu *et al.* [2017] reported some interesting Equatorial Plasma Bubbles (EPBs) on 4 and 5 October 2013, and 29 and 30 September 2013. The EPBs had planar wave-like structures and their wavefronts were parallel to each other before midnight. The angle between the wavefronts of those EPBs and the geomagnetic meridian were about 30°. Near midnight, one of the all-sky airglow imagers detected an unusual C-shaped EPB for the first time.

Known as “Third Pole” of the Earth, with it important influences on global climates and local weather, the Tibetan Plateau (TP) area has become a focus of space environment study. To investigate how orographic features of the TP affect the geographical distributions of Gravity Wave (GW) sources, Li *et al.* [2016] studied the characteristics of GWs over the southeastern TP region using three-year OH airglow images from Qujing. They found that most of GWs exhibited ducted or evanescent characteristics. Almost all GWs propagated southeastward in winter. The GW propagation directions in winter differed significantly from other airglow imager observations at northern middle latitudes. They also found that most of the mesospheric freely propagating GWs were located in or near the large wind shear intensity region (10–17km) on the southeastern edge of the TP in spring and winter. This work provides valuable information for the GW parameterization schemes in general circulation models in TP region.

3.2 Coupling between Space Spheres at Different Heights

The layers of Earth's upper atmosphere, ionosphere, and magnetosphere form a closely-coupled interacting system. The solar wind interaction with the earth’s magne-

tosphere and ionosphere, while the lithosphere and hydrosphere interaction with atmosphere and ionosphere. The Meridian Project uses multiple instruments to monitor atmosphere, ionosphere, magnetosphere, and interplanetary space, providing a good opportunity to research the spheres coupling. In recent years, scientists made considerable achievements in research of spheres coupling by using the Meridian Project data.

Ouyang *et al*. [2016] used data from ground-based magnetometers and HF Doppler sounder to study the UltraLow Frequency (ULF) waves excited during the storm sudden commencement (SSC) on 8 March 2012 and they found a possible evidence on the link between ULF waves and ionospheric Doppler shifts. Ionospheric Doppler shift could response to ULF oscillations in magnetic field in various frequency ranges, especially in the frequency range of Pc3–Pc4 and below. This study demonstrated a new mechanism of magnetosphere-ionosphere coupling.

Zhang *et al*. [2016] reported a case of continuous monitoring of a polar cap patch by a network of HF radars and TEC (total electron content) monitors. The results showed the initial anti-sunward motion of the polar cap patch was halted due to a rapidly changing of Interplanetary Magnetic Field (IMF) from strong southward to strong eastward with weaker northward components. Then the patch very slowly evolved behind the duskside of a lobe reverse convection cell in afternoon sectors, accompanied by high-latitude lobe reconnection, subsequently fading rapidly due to an enhancement of the ionization recombination rate. This differed from the classic scenario where polar cap patches were transported across the polar cap along the stream lines of a twin-cell convection pattern from day to night. This observation provides new important insights into patch formation and their dependence on IMF. It helps us to understand better solar wind-magnetosphere-ionosphere coupling.

Hao *et al*. [2017] found a new type of TEC variation when an interplanetary shock impacted on the Earth's magnetosphere on 17 March 2015. Their study suggested that the TEC variation was caused by shock-induced magnetospheric compression, which moved plasma earthward in the dayside plasmasphere. As a result, some plasma outside of GPS satellite orbit was moved to the inside and contributed to the plasma content traversed by GPS ray path. This result indicates that the magnetospheric compression plays an important role in solar wind -magnetosphere-ionosphere coupling.

Ionospheric responses to Sudden Stratospheric Warming (SSW) are not well understood, particularly in mid-latitude regions and under high solar conditions. Chen *et al*. [2016] studied the mid-latitude ionospheric responses to the 2013 SSW. During the 2013 SSW, ionospheric disturbances were observed at eight locations on the meridional chain from 30.5°N to 42.8°N in northern China. The amplified diurnal, semidiurnal, and terdiurnal tides in f_0F_2 can be recognized during the SSW. Importantly, the variations in the semidiurnal tides included a 16 day periodic component, indicating that the modulated semidiurnal tides may transmit these 16 day planetary wave-like oscillations to the F region through wind dynamo. The coupling between the atmosphere and ionosphere may be strengthened by the quasi-16 day waves.

Lei *et al*. [2016] investigated the responses of the F_2 peak and the topside ionosphere to the 2 October 2013 geomagnetic storm, using data from ionosondes, ground-based GPS receivers, Gravity Recovery and Climate Experiment (GRACE) and MetOp-A satellites, and Fabry-Perot interferometer over the Asian-Australian sector. It was found that the upward looking TEC from Low-Earth Orbit (LEO) satellites did not undergo such depletions as seen in the region near the F_2 peak, and they even showed increases. Simulation results and observations indicated that the contrasting behavior of the F_2 peak and the topside ionosphere were mainly associated with the enhancement of the equatorward winds, albeit the disturbed electric fields

Kuai *et al*. [2017] studied regional differences of the ionospheric response to the July 2012 geomagnetic storm by multiple instrumental observations. They found both the topside ion concentrations and TEC presented a remarkable hemispheric asymmetry, mainly resulting from the asymmetry in neutral winds and composition disturbances. The studies of Lei *et al*. [2016] and Kuai *et al*. [2017] can help us to learn more about the influence of winds in ionosphere-atmosphere coupling, and they are very important for establishing accurate model.

Atomic sodium (Na) is one of the major meteoric species existing as layers of atoms in the Mesosphere/Lower Thermosphere (MLT) at altitudes of 80–105 km and atomic ions at higher altitudes. As the

boundary between neutral atmosphere and ionosphere, the MLT region is of particular interest because it is influenced by the mesoscale convective weather and thunderstorms from below and exposed to solar radiation from above. Yu *et al*. [2017] presented observational results on a statistical basis showing evidence that thunderstorm activities could affect the metal layer, by identifying a statistically significant enhancement of the neutral metal Na layer above thunderstorms at Haikou, China. The thunderstorm-generated gravity waves and electric field effects could be the mechanisms responsible for the lightning-associated enhancement of Na layer. The influence of thunderstorms on metallic species would significantly enhance our understanding of how atmosphere interacts with ionosphere.

Ionospheric disturbances excited by strong shallow earthquakes are important, as they can reveal information about Lithosphere-Atmosphere-Ionosphere Coupling. Using TEC data from GPS stations, Liu *et al*. [2017] studied the response of the Coseismic Ionospheric Disturbances (CIDs) following the M_w 7.8 Gorkha inland earthquake which occurred on 25 April 2015. The CIDs observed could be classified into three groups: CIDs related to Gravity Waves (GWs), CIDs related to Acoustic Waves (AWs), and CIDs related to seismic Rayleigh surface waves. Through comparing the seismogram data from Incorporated Research Institutions for Seismology to the TEC data, they found that the azimuthal characteristics of the ground vibrations agreed with the directivity of the CIDs related to Rayleigh surface waves.

3.3 Space Weather Disturbance and its Propagation

Equatorial Plasma Bubbles (EPBs) are depleted regions of plasma density that align with the geomagnetic field lines. They are common disturbances that frequently occur in nighttime ionosphere.

All-sky airglow imagers of the Meridian Project could been used to visualize the horizontal structures of EPBs. Sun *et al*. [2016] investigated the statistical features of EPBs using the instruments in the equatorial region of China. They found that EPBs mainly occur during 21:00 LT–00:00 LT in equinoxes. Most EPBs occurred in groups of two to six depletions. The average distance between adjacent EPB depletions was 200–300 km. The zonal extension of an EPB group was usually less than 1500 km. EPBs usually had a maximum drift velocity near 100 m/s at 21:00 LT–22:00 LT in equatorial region and then decreased to 50–70 m/s toward sunrise. The averaged westward tilt angle of most EPBs (with respect to the geographic north-south) increased from 5°–10° to 23°–30° with LT between 20:00 and 03:00 LT, then decreased to 10°–20° toward sunrise. The EPB occurrence patterns and zonal drift velocities are significantly different from those at Kolhapur, India, which locates west to the stations in their study by 20.0°–32.0°in longitude.

Sun *et al*. [2017] for the first time reported the evolution processes of a group of EPBs that were simultaneously observed by two all-sky airglow imagers, a Digisonde, a VHF radar, and the C/NOFS satellite in the Chinese longitudinal sector. The airglow depletion structures seen by all-sky airglow imagers had the same zonal wavelength as that of the longitudinally periodic electron density depletions observed by the C/NOFS satellite. Results also indicated that the EPB group developed from the bottom side Large-Scale Wave-like Structure (LSWS) at about 195–210 km height with a characteristic zonal wavelength and longitudinal extension of about 450 km and 2250 km, respectively. The EPB group also caused periodic bottom side type spread F associated with the LSWS. It is found that the development of the EPB group and their associated spread F could be limited by the equatorward motion of Equatorial Ionization Anomaly (EIA) and the Southwestward Motion of an Extremely Bright Airglow Region (SMEBAR). Both EIA and SMEBAR could feed high plasma density into an EPB airglow depletion structure that was eventually seen as a bright airglow structure or disappeared.

Wu *et al*. [2017] reported interesting results of EPBs observed by two all-sky imagers located in the magnetically equatorial region of Hainan and Guiping, China. The EPBs of 4 and 5 October 2013 had planar wave-like structures and their wave fronts were parallel to each other before midnight. The angle between the wave fronts of those EPBs and the geomagnetic meridian were about 30°. Near midnight, the higher-latitude part of this EPB suddenly rotated, forming an unusual C-shaped EPB. After midnight, this EPB merged into another EPB and formed an integrated EPB. The other EPB case on 29 and 30 September 2013 showed the full evolution processes of an “I” shaped EPB. The imagers

also observed “S” and “Y” shaped EPBs. The change of EPBs’ shape was directly related to the change of EPBs’ zonal drift velocities. The study proposed that the angle between the I-shaped EPBs and the geomagnetic meridian was likely caused by the change of the latitudinal gradient of zonal neutral wind velocities and ionospheric conductivity. More interestingly, they found that the location of Atmosphere Gravity Wave (AGW) source was consistent with the center of a concurring typhoon. This indicates that the AGWs might be caused by the typhoon.

During geomagnetic storms, intense energy input from the magnetosphere perturbs the ionosphere on a global scale through high-latitude ionization, Joule heating, ion-drag forcing, and even direct electric field penetration. The global ionosphere and thermosphere response to geomagnetic storms have been extensively investigated through observations or according simulations of the Meridian Project.

Yue *et al*. [2016] used an ionospheric electron density reanalysis algorithm to generate global optimized electron density during a geomagnetic storm. The reanalyzed electron density identified large-scale ionospheric features quite well during storm time, including the storm-enhanced density, the positive ionospheric storm effect during the initial and main phases, and the negative ionospheric storm effect during the recovery phase. The simulations from the Thermosphere Ionosphere Electrodynamics General Circulation Model reproduced similar large-scale ionospheric disturbances. Both the reanalysis and simulations showed long-lasting (>17 h) daytime negative storm effect over the Asia sector as well as hemispheric asymmetry during the recovery phase. Detailed analysis of the Global Ultraviolet Imager-derived O/N_2 ratio and model simulations indicated that the polar ward meridional wind disturbance, the downward E×B drift disturbance and O/N_2 depletion might be responsible for the negative storm effect. The hemispheric asymmetry is mainly caused by the geomagnetic field line configuration, which could cause hemispheric asymmetry in the O/N_2 depletion.

Kuai *et al*. [2016] revealed that the disturbed electric fields, which comprise Penetration Electric Fields (PEFs) and Disturbance Dynamo Electric Fields (DDEFs), played a decisive role in the ionospheric storm effects in low latitude and equatorial regions. Observations showed both the DDEFs and PEFs presented a notable local time dependence, which caused sector differences in the characteristics of the disturbed electric fields. This differences further lead to the sector differences in the low-latitude ionospheric response during the storm. Kuai *et al*. [2017] found regional differences of the ionospheric response to the geomagnetic storm. In the Asian-Australian sector, an intensive negative storm was detected near longitude 120°E, and in the topside ionosphere the negative phase mainly existed in the equatorial region. The topside and bottom side TEC contributed equally to the depletion of TEC. The positive storm effects were stronger at the Eastside than at the Westside. The topside TEC made a major contribution to the enhancement in TEC for the positive phases, showing the important role of the equatorward neutral winds. For the American sector, the equatorial ionization anomaly intensification was stronger in the Westside than in the Eastside and showed the strongest feature in the longitude ~110°W. The combined effects of the disturbed electric fields, composition disturbances, and neutral winds caused the complex storm time features.

The spatially and temporally variable ionosphere significantly affects the accuracy and reliability of radio communications. Li *et a*l. [2017] found that the Bottom-type irregularity Scattering Layer (BSL) in the ionospheric F region bottom-side after sunset served as a possible telltale of Equatorial Spread F (ESF). Using simultaneous multi-beam radar measurements over two low-latitude stations, Sanya and Fuke in China, they reported, for the first time, a thin BSL that initially occurred at pre-sunset, much earlier than the occurrence of BSL generated from the equatorial plasma shear vortex-driven instability. The pre-sunset BSL was situated around 225 km altitude and continued to exist until the appearance of ESF plumes after sunset. Interestingly, the Doppler velocities of the pre-sunset BSL echoes measured by the radar and the F layer virtual heights obtained from the collocated Digisonde measurements over Sanya both showed oscillations with a period of about 1 h, suggesting a close link between the occurrences of the BSL and that of F region plasma density large-scale wave structure before sunset. These observations implied an important role of gravity waves in the generation of the pre-sunset F region bottom-type irregularities.

Chen *et al*. [2017] reported a case of extremely rare

daytime F region irregularities at noon. In that case, two Field-Aligned Irregularities (FAIs) appeared in the topside F_2 layer and presented small Doppler velocities and narrow spectral widths. The FAIs moved northward with almost no zonal speed. The irregularities emerged in the geomagnetically quiet condition and were irrelevant to the storm-induced eastward electric field as other daytime cases. More than 2 h after the emergency of the daytime irregularities over Hainan, the Shaoyang digisonde situated about 870 km north to the HCOPAR recorded the spread-F in ionospheric F1 layer. According to the echo altitudes, the spread-F may connect the daytime bubbles via magnetic field line. The strong photoionization after sunrise made it difficult to generate the plasma bubbles in the sunlit ionosphere. Consequently, the two midday FAIs over Hainan may drift along the magnetic field lines from higher altitudes in the south and were most likely the remnant of previous night's bubbles.

3.4 Space Weather Effects on Ground Facilities

Geomagnetically Induced Currents (GICs) in long-distance conductive ground infrastructures such as pipelines, communication cables, and high-voltage power transmission systems are harmful to those facilities. Large GICs are usually observed at high-latitude locations due to large magnitude and highly variable geomagnetic field disturbance caused by intensification of ionospheric electrojets in association with substorms. Thus GIC had been considered as a particular high-latitude problem for a long time. However, there were reports that GIC can disrupt the power networks at lower latitudes in extreme events.

Zhang *et al*., [2015] reported an event in which the GIC due to SSC was 2 or 3 times higher than that during storm main phase. Further analysis about the GIC index derived from the geomagnetic observations implied that this phenomenon was more remarkable at low-latitude sites, which demonstrated the important role of the SSC events played in inducing GIC at low-latitude. In addition, the PPMLR-MHD model of the Meridian Project was used to predict the GIC caused by the SSC event of 17 March 2015 at the two Chinese GIC-monitoring sites by using the solar wind conditions observed by the Wind satellite as input. The model reproduced the main geomagnetic variations pretty well and generally captured the main feature of recorded GIC. This method provided a short lead time GIC forecast for the low-latitude power networks when the upwind satellite observed an interplanetary shock. This is the first try for the model to carry out forecast of GIC at low-latitude locations caused by the SSC event.

Following the previous work, Zhang *et al*. [2016] provided a risk assessment of effects of extreme interplanetary shocks on low-latitude power networks. The extreme interplanetary shock of 23 July 2012 was simulated under the assumption that it had hit the Earth and the shock-caused SC would be 123 nT. During this extreme event, the simulation indicates that dB/dt, which was usually used as a proxy for GICs, at a dayside low-latitude substation would exceed 100 nT/min. This is very large for low-latitude regions. The GIC threat level based on the simulated geomagnetic perturbations was assessed by using the Marshall method. The results indicated that the risk remained at "low" level for the low-latitude power network on a global perspective. However, the GIC risk may reach "moderate" or even "high" levels for some equatorial power networks due to the influence of the equatorial electrojet. Results of this study featured substantial implications for risk management, planning, and design of low-latitude electric power networks.

So far, most of the research on the GICs concerns electrical systems and pipelines, while less is known about the effects of geomagnetic storm on the railway system. There were a few reports that geomagnetic storms could cause anomalies in the signaling and control system [Liu *et al*., 2015]. To study the impact of geomagnetic storm on the equipment of traction electrification system in the high-speed railway [Liu *et al*., 2016], Geomagnetically Induced Current (GIC) monitoring devices were installed in the Hebi East traction power supply substation of the Beijing-Hong Kong Dedicated Passenger Line, and GICs were captured during two geomagnetic storms on 17 March and 23 June 2015. The analysis of the monitor data showed a good agreement between the GIC captured on 17 March and the geomagnetic data obtained from the Malingshan Geomagnetic Observatory of the Meridian Project. The correlation is significant between the measured currents and the geomagnetic field component variations B_x and B_y. In other words, the geomagnetic field variation should be responsible for a significant part of the currents captured in the railway system.

4. Outlook and Further Development

4.1 Phase II of the Chinese Meridian Project

For the current Meridian Project, as limited by a small budget, no solar observation capability was built, a large area of China's territory is not covered, distances between adjacent stations are too large for study of medium to small scale phenomena, and the capability of the ordinary instruments adopted by the current project is still relatively weak. A major upgrade to the current Meridian Project is strongly demanded.

Actually, even before construction of the Meridian Project was completed, Phase II of the project was proposed. Significant progresses have been made since Chinese government began to make its 13th Five-Year Plan (2016 to 2020) on major scientific infrastructure construction projects. The phase II of the Meridian Project was officially listed among the 10 projects with highest priority for the Five-Year Plan. Now the proposal of the new project has been approved by China's National Development and Reform Commission. The construction is scheduled to start at the end of 2018 and complete in 2022.

Phase II of the Meridian Project will add to the current project two observatory chains, one along 100°E and another along 40°N. Together with the current 120°E and 30°N chains, a two-cross network configuration will be formed to cover nearly the whole territory of China in a sense of monitoring medium scale phenomena, and distances between adjacent stations will be as small as 100km in some critical regions. Also, a series of solar-interplanetary monitoring instruments will be added to constitute a complete observation capability that covers all spheres of the solar-terrestrial system, including solar surface, interplanetary space, magnetosphere, ionosphere, and atmosphere. Aside from general-purpose small instruments that constitute the network, the Meridian Project phase II plans to set up 4 key monitoring regions: the polar region, north frontier of China, Tibetan Plateau and the South of China. A number of large-scale instruments will be built to make comprehensive and delicate observation in these four regions. Among these large-scale instruments, the three-station mode incoherent scatter radar in Hainan, the multi-station mid-latitude HF radar array in northern China and a series of solar radio imaging devices will be most prominent. Altogether, about 200 new instruments will be deployed or built, and the number of stations will increase from 15 to 31 (see Figure 2).

4.2 International Space Weather Meridian Circle Program

On the basis of the Meridian Project, Chinese scientists had proposed International Space Weather Meridian Circle Program (IMCP). IMCP is intended to connect 120°E and 60°W chains of ground-based monitors all over the world, which will enhance the ability of scientists to monitor the space environment worldwide. The 120°E/60°W meridian circle is the best option for ground observation, since most portion of it is located on land.

To date, multiple universities or institutions from Australia, Brazil, Canada, Russia, and the United State keep in contact with China on IMCP and have shown great interest. As the first substantial step of IMCP, China and Brazil setup a joint laboratory for space weather monitoring and research. In 2017, the laboratory completed its all construction tasks mainly including several instruments and a data center, and began to have a test run.

The 2017 International Meridian Circle Program (IMCP) workshop was held in Qingdao, China, during May 15-18, 2017. Scientists from more than 11 countries made consensus to establish an International Meridian Organization (IMO) in Beijing to further promote and coordinate cooperative activities.

In 2017, as a part of an effort of China to lead or join international science programs, IMCP was updated and a new proposal was submitted to the Ministry of Science and Technology of China. Named Major Scientific Program of International Meridian Circle, the program would focus on international joint space weather research, aiming at alleviating disastrous effects on modern society (see Figure 2).

5. Conclusion

In recent two years, using data from the Chinese Meridian Project, significant progresses have been made in space weather and space physics research. Here we summarized these achievements into 4 categories: regional characteristics of space environment above China or along 120°E meridian line, coupling between space

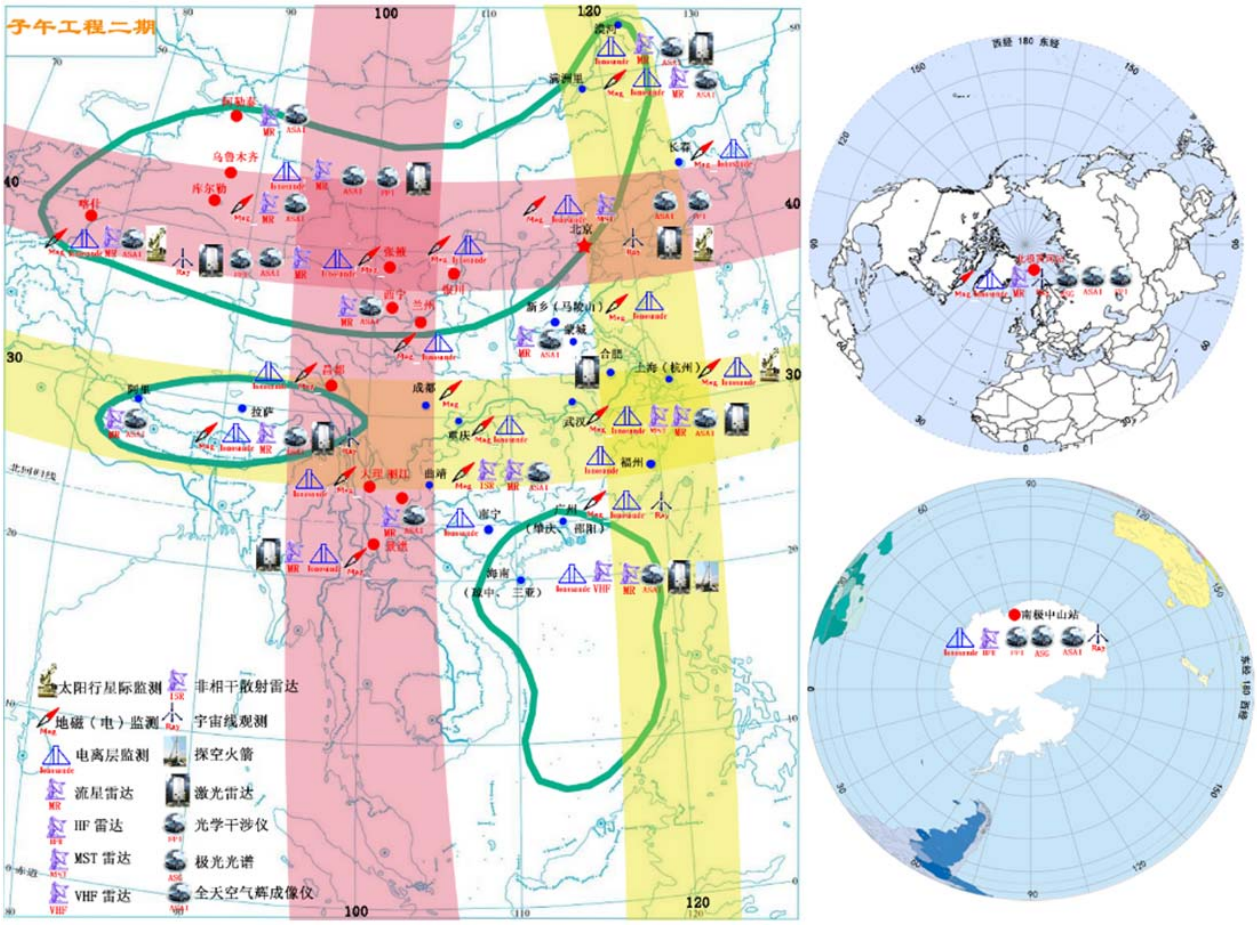

Fig. 2 The initial deployment of stations and instruments of phase II of Meridian Project

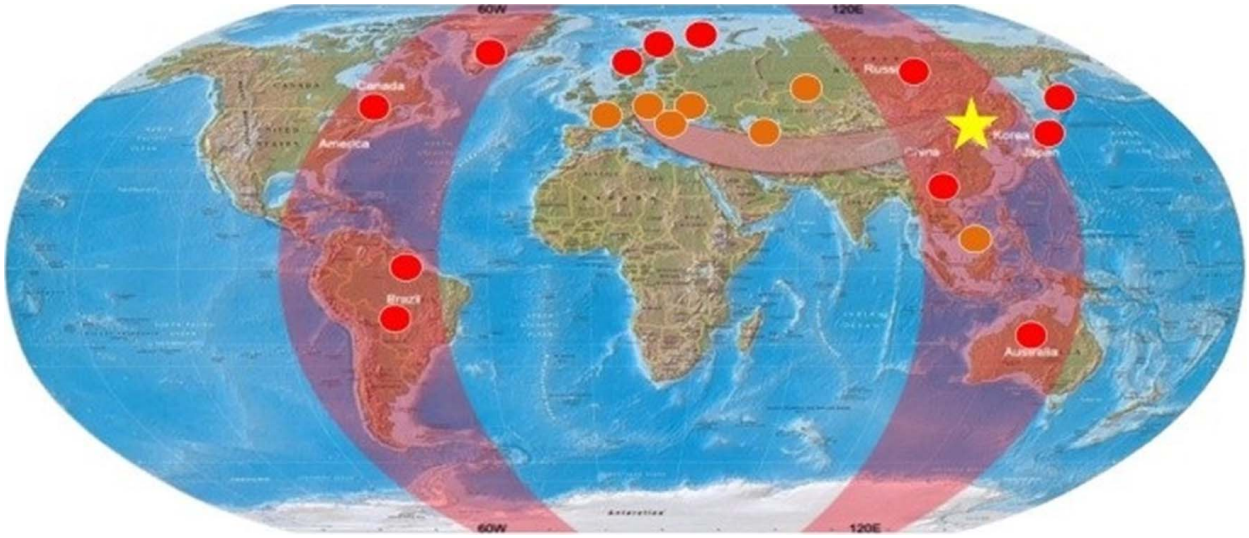

Fig. 3 Preliminary layout of instruments proposed by Major Scientific Program of International Meridian Circle

spheres at different heights, space weather disturbance and its propagation, and space weather effects on ground technical facilities.

Aside from research progresses, China took huge paces to build a world leading ground-based space environment monitoring system, named phase II of the

Meridian Project. Meanwhile, as IMCP coming into realization, it is strongly expected that China will play a more and more important role in the international space weather community.

References

[1] Chen, G., C. Wu, S. Zhang, B. Ning, X. Huang, D. Zhong, H. Qi, J. Wang, and L. Huang (2016), Mid-latitude ionospheric responses to the 2013 SSW under high solar activity. J. Geophys. Res. Space Physics, 121, 790 –803, doi:10.1002/ 2015JA021980

[2] Chen, G., *et al*. (2017), Low-latitude daytime F region irregularities observed in two geomagnetically quiet days by the Hainan coherent scatter phased array radar (HCOPAR), J. Geophys. Res. Space Physics, 122, 2645–2654,doi:10.1002/2016JA023628

[3] Chi Wang (2010), New Chains of Space Weather Monitoring Stations in China, Space Weather, Vol. 8, S08001, doi:10.1029/ 2010SW000603

[4] Hao, Y., J. Huang, W. Liu, D. Zhang, and Z. Xiao (2017), Prompt GPS TEC response to magnetospheric compression. J. Geophys. Res. Space Physics, 122, 4357–4366, doi:10.1002/2017JA023866

[5] Huang, C., Zhang, S., Chen, G., Zhang, S. & Huang, K. (2017). Planetary wave characteristics in the lower atmosphere over Xianghe (117.00°E, 39.77°N), China, revealed by the Beijing MST radar and MERRA data. Journal of Geophysical Research: Atmospheres, 122, 9745–9758, doi:10.1002/2017JD027029

[6] Jiao, J., G. Yang, J. Wang, W. Feng, and J. M. C. Plane (2017), Observations of dramatic enhancements to the mesospheric K layer, Geophys. Res. Lett, 44, 12,536–12,542, doi: 10.1002/2017GL-075857

[7] Kuai, J., L. Liu, J. Lei, J. Liu, B. Zhao, Y. Chen, H. Le, Y. Wang, and L. Hu (2017), Regional differences of the ionospheric response to the July 2012 geomagnetic storm, J. Geophys. Res. Space Physics, 122, doi:10.1002/2016JA023844

[8] Kuai, J., L. Liu, J. Liu, S. Sripathi, B. Zhao, Y. Chen, H. Le, and L. Hu (2016), Effects of disturbed electric fields in the low-latitude and equatorial ionosphere during the 2015 St. Patrick's Day storm, J. Geophys. Res. Space Physics, 121, 9111–9126, doi:10.1002/ 2016JA022832

[9] Lei, J., *et al*. (2016), Contrasting behavior of the F2 peak and the topside ionosphere in response to the 2 October 2013 geomagnetic storm, J. Geophys. Res. Space Physics, 121, 10,549–10,563, doi:10.1002/2016JA022959.

[10] Li, R., T. Chen, F. Man, *et al*. (2016), Characteristics of low altitude ionospheric electric field over Hainan Island, China, Sci. China Earth Sci., 60, 770, doi:10.1007/s11430-016-0123-5

[11] Li, Q., J. Xu, X. Liu, W. Yuan, and J. Chen (2016), Characteristics of mesospheric gravity waves over the southeastern Tibetan Plateau region, J. Geophys. Res. Space Physics, 121, 9204–9221, doi:10.1002/2016JA022823

[12] Li, G., B. Ning, M. A. Abdu, W. Wan, C. Wang, G. Yang, K. Liu, L. Liu, and C. Yan (2017), First observation of pre-sunset ionospheric F region bottom-type scattering layer, J. Geophys. Res. Space Physics, 122, 3788–3797, doi:10.1002/2016JA023647.

[13] Liu, H., F. Ding, B. Zhao, J. Li, L. Hu, W. Wan, and B. Ning (2017), Ionospheric response following the Mw 7.8 Gorkha earthquake on 25 April 2015, J. Geophys. Res. Space Physics, 122, 6495–6507, doi:10.1002/2016JA023079

[14] Liu, L., H. Liu, Y. Chen, H. Le, Y.-Y. Sun, B. Ning, L. Hu, and W. Wan (2017a), Variations of the meteor echo heights at Beijing and Mohe, China, J. Geophys. Res. Space Physics, 122, 1117–1127, doi:10.1002/2016JA023448

[15] Liu, L., H. Liu, H. Le, Y. Chen, Y.-Y. Sun, B. Ning, L. Hu, W. Wan, N. Li, and J. Xiong (2017b), Mesospheric temperatures estimated from the meteor radar observations at Mohe, China, J. Geophys. Res. Space Physics, 122, 2249–2259, doi:10.1002/2016JA023776

[16] Liu, L., X. Ge, W. Zong, Y. Zhou, and M. Liu (2016), Analysis of the monitoring data of geomagnetic storm interference in the electrification system of a high-speed railway, Space Weather, 14, doi:10.1002/2016SW001411

[17] Ouyang, X., W. Liu, Z. Xiao, and Y. Hao (2016), Observations of ULF waves on the ground and ionospheric Doppler shifts during storm sudden commencement, J. Geophys. Res. Space Physics, 121, 2976–2983, doi:10.1002/ 2015JA022092

[18] Qiu, S. C, Y. H. Tang, M. J. Jia, X. H. Xue, X. K. Dou, T. Li, and Y. H. Wang (2016), A review of latitudinal characteristics of sporadic sodium layers, including new results from the Chinese Meridian Project, Earth-Science Reviews, 162, 83-106, doi:10.1016/j.earscirev.2016.07.004

[19] Sun, L., J. Xu, W. Wang, W. Yuan, Q. Li, and C. Jiang (2016), A statistical analysis of equatorial plasma bubble structures based on an all-sky airglow imager network in China, J. Geophys. Res. Space Physics, 121, 11,495–11,517, doi:10.1002/2016JA022950

[20] Sun, L., J. Xu, W. Wang, W. Yuan, and Y. Zhu (2017), Evolution processes of a group of equatorial plasma bubble (EPBs) simultaneously observed by ground-based and satellite measurements in the equatorial region of China, J. Geophys. Res. Space Physics, 122, doi:10.1002/2016JA023223

[21] Wang, Z., G. Yang, J. Wang, C. Yue, Y. Yang, J. Jiao, L. Du, X. Cheng, and W. Chi (2017), Seasonal variations of meteoric potassium layer over Beijing (40.41°N, 116.01°E), J. Geophys. Res. Space Physics, 122, doi:10.1002/ 2016JA023216

[22] Wu, K., Xu, J., Wang, W., Sun, L., Liu, X., & Yuan, W. (2017). Interesting equatorial plasma bubbles observed by all-sky imagers

in the equatorial region of China. Journal of Geophysical Research: Space Physics, 122. https://doi.org/10.1002/2017JA024561

[23] Wu, C., and F. Yi (2017), Local ice formation via liquid water growth in slowly ascending humid aerosol/liquid water layers observed with ground-based lidars and radiosondes, J. Geophys. Res. Atmos., 122, doi:10.1002/2016JD025765

[24] Yu, B., X. Xue, G. Lu, *et al*. (2017), The enhancement of neutral metal Na layer above thunderstorms, Geophys. Res. Lett, 44, doi:10.1002/2017GL074977

[25] Yu, T., C. Xia, X. Zuo, C. Huang, T. Mao, L. Liu, and Z. Liu (2016), A comparison of mesospheric and low-thermospheric winds measured by Fabry-Perot interferometer and meteor radar over central China, J. Geophys. Res. Space Physics, 121, 10,037–10,051, doi:10.1002/ 2016JA022997

[26] Yue, X., W. Wang, J. Lei, A. Burns, Y. Zhang, W. Wan, L. Liu, L. Hu, B. Zhao, and W. S. Schreiner (2016), Long-lasting negative ionospheric storm effects in low and middle latitudes during the recovery phase of the 17 March 2013geomagnetic storm, J. Geophys. Res. Space Physics, 121, doi:10.1002/2016JA022984

[27] Zhang, J. J., C. Wang, T. R. Sun, C. M. Liu, and K. R. Wang (2015), GIC due to storm sudden commencement in low-latitude high-voltage power network in China: Observation and simulation, Space Weather, 13, 643–655, doi:10.1002/2015SW001263

[28] Zhang, J. J., C. Wang, T. R. Sun, and Y. D. Liu (2016), Risk assessment of the extreme interplanetary shock of 23 July 2012 on low-latitude power networks, Space Weather, 14, 259–270, doi:10.1002/2015SW001347

[29] Zhang, Q.-H., *et al*. (2016), Polar cap patch transportation beyond the classic scenario, J. Geophys. Res. Space Physics, 121, 9063–9074, doi:10.1002/ 2016JA022443

[30] Zhou, C., Q. Tang, X. Song, H. Qing, Y. Liu, X. Wang, X. Gu, B. Ni, and Z. Zhao (2017), A statistical analysis of sporadic E layer occurrence in the mid-latitude China region, J. Geophys. Res. Space Physics, 122, 3617-3631, doi:10.1002/ 2016JA023135